Science Advances

AAAS

Supplementary Materials for

Microscopic pathways for stress relaxation in repulsive colloidal glasses

F. Dallari*, A. Martinelli*, F. Caporaletti, M. Sprung, G. Grübel, G. Monaco*

*Corresponding author. Email: francesco.dallari@desy.de (F.D.); a.martinelli-2@unitn.it (A.M.);
giulio.monaco@unitn.it (G.M.)

This PDF file includes:

Supplementary Materials

Section S1. X-ray photon correlation spectroscopy

In X-Ray Photon Correlation Spectroscopy (XPCS) experiments a beam of (partially) coherent X-rays of wavelength λ impinges on the sample and the scattered photons are collected at a given exchanged wave-vector, q, where $q = \frac{4\pi}{\lambda}\sin(\theta/2)$ and θ is the scattering angle. The scattered radiation is often sampled with a multi-element detector and a sequence of images is collected at times t. As in visible dynamic light scattering (*40*), the normalised auto-correlation function of the scattered intensity, $I(q,t)$, is then calculated

$$g_2(q,t) = \frac{\langle I(q,0)I(q,t)\rangle}{\langle I(q,t)\rangle^2} \tag{1}$$

where $\langle...\rangle$ is an average over the pixels of the detector and/or over time. If the scattered electric field, $E(q,t)$, is a zero mean Gaussian complex variable, Eq. 1 can be written as

$$g_2(q,t) = 1 + \alpha(q)\left|\frac{\langle E^*(q,0)E(q,t)\rangle}{\langle I(q)\rangle}\right|^2 \tag{2}$$

where $\alpha(q)$ is a parameter, known as contrast, comprised between zero and one that depends on the experimental setup. Typically in XPCS experiments carried out at third generation synchrotron sources $\alpha(q)$ can be a small number due to the partial coherence of the X-ray beam (*41*). Eq. 2 is known as the Siegert relation and allows relating the intensity auto-correlation function via the electric field correlation function to the intermediate scattering function, $F(q,t)$

$$g_2(q,t) = 1 + \alpha(q)\left|\frac{F(q,t)}{F(q,0)}\right|^2 \tag{3}$$

The intermediate scattering function is the density-density correlation function, i.e.

$$F(q,t) = \langle \rho_q^*(0)\rho_q(t)\rangle \tag{4}$$

where $\rho_q(t)$ is the q component of the microscopic density at time t. Therefore, XPCS experiments provide direct access to the density-density correlation function.

Section S2. Sample characterization

The sample preparation procedure is presented in the Methods. Here, its characterisation in terms of volume fraction and structure is discussed.

Volume fraction measurements

The volume fraction of the samples cannot be evaluated precisely from the procedure discussed in the Methods, and has to be measured directly. X-ray transmission provides a tool to achieve this. In fact, according to the Lambert-Beer equation, the transmitted intensity can be expressed as

$$I(y) = I_0 \exp\left[-\left(s(y)/\mu_{capillary} + L(y)\varphi/\mu_{SiO_2} + L(y)(1-\varphi)/\mu_{WL}\right)\right] \tag{5}$$

where y is the horizontal coordinate orthogonal to the beam direction; $I(y)$ is the transmitted intensity with the sample at position y; I_0 is the incoming beam intensity; $s(y)$ is the thickness of the two capillary walls at position y traversed by the X-ray beam; $L(y)$ is the thickness of the traversed sample; φ is the volume fraction; $\mu_{capillary}$, μ_{SiO_2} and μ_{WL} are the absorption lengths of the capillary (borosilicate glass), silica (nanoparticles) and water-lutidine solution, respectively. The water-lutidine absorption length was estimated using the relation: $1/\mu_{WL} = C_L^v/\mu_{lutidine} + (1 - C_L^v)/\mu_{H_2O}$, where $C_L^v = 0.265 \pm 0.010$ is the volume fraction of lutidine in the solution, $\mu_{H_2O} = 1030 \quad \mu m$, $\mu_{lutidine} = 2553 \quad \mu m$ (42). Moreover, we used $\mu_{capillary} = 136 \quad \mu m$ and $\mu_{SiO_2} = 143 \quad \mu m$ (42). A transmission measurement can then provide φ.

An example of a transmission measurement is reported in Fig. S1A and the corresponding volume fraction extracted inverting Eq. 5 in Fig.S1B. The latter plot demonstrates the homogeneity of the sample, and provides $\varphi = 37.65\%$. The volume fraction measurement has a standard deviation of 0.11% over the horizontal section shown in Fig. S1B. For what concerns the absolute value of the volume fraction, we estimate an error of 0.2% due to residual uncertainties in the parameters entering Eq. 5, the most severe of which concerns the capillary wall thickness.

Scans at different heights of the sample were also carried out to assess the absence of sedimentation.

Form factor and structure factor

The scattered intensity can be written as $I(q) \propto S(q)|f(q)|^2$. Here $f(q)$ is the form amplitude, $|f(q)|^2$ is the form factor and $S(q)$ is the static structure factor

$$S(q) = F(q, 0) = \langle \rho_q^*(0)\rho_q(0) \rangle \tag{6}$$

The form factor can be obtained directly measuring the intensity scattered by a low volume fraction solution where $S(q) = 1$ with very good approximation. In the present experiment, a solution with volume fraction $\phi_r < 0.001$ was used. The corresponding experimental data are
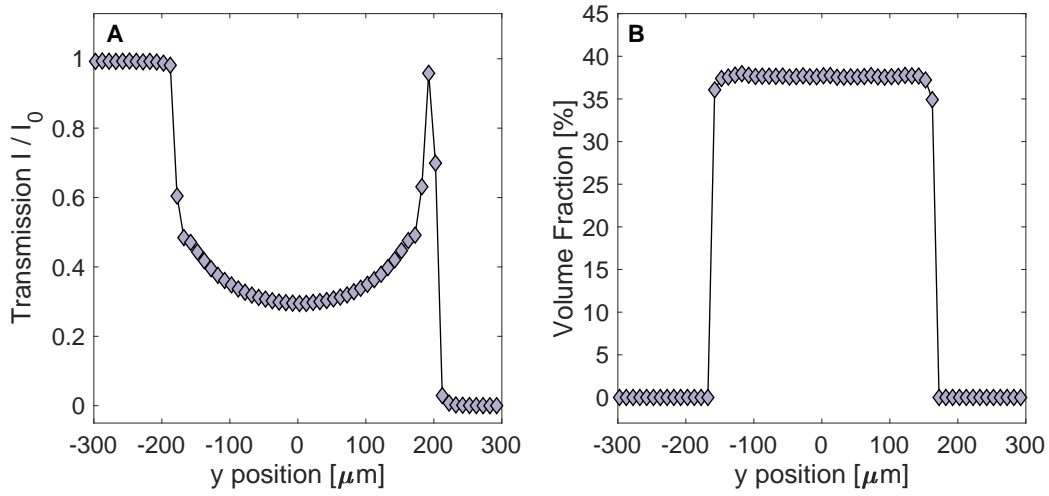
Fig. S1. Volume fraction measurement. A) Transmission scan for the sample reported as the ratio of the transmitted to the incoming beam intensity as a function of the sample position y transverse to the incoming beam direction. **B)** Volume fraction obtained from Eq. 5 as a function of y.

reported in Fig.S2 (green circles) together with a fit carried out assuming a Schultz distribution to describe the polydispersivity of the nanoparticles (*43*). The result of the fitting procedure gives an average radius of $\bar{R} = (50.8 \pm 0.3)$ nm and a polydispersity $\frac{\Delta r}{R} = (9.4 \pm 0.6)\%$. The intensity scattered from the sample is reported as a function of q in Fig. S2 as red diamonds. The experimental structure factor $S(q)$ can be obtained as $I(q)/|f(q)|^2$ (inset in Fig.S2)

The structure factor calculated at the beginning (green diamonds) and at the end (red circles) of the measurements discussed in the main text is reported in Fig. S3. During the measurement time (lasted ≈600 s) there is no sign of a change of the structural properties.

Section S3. Dynamical properties

In SAXS geometry, rings on the detector centred at the transmitted beam position correspond to a given $|\mathbf{q}|$, and the pixels over a given ring can be identified by an angle ϕ, where we define this angle with respect to the horizontal direction (see Fig. 1A in the main text). In Fig. S4A
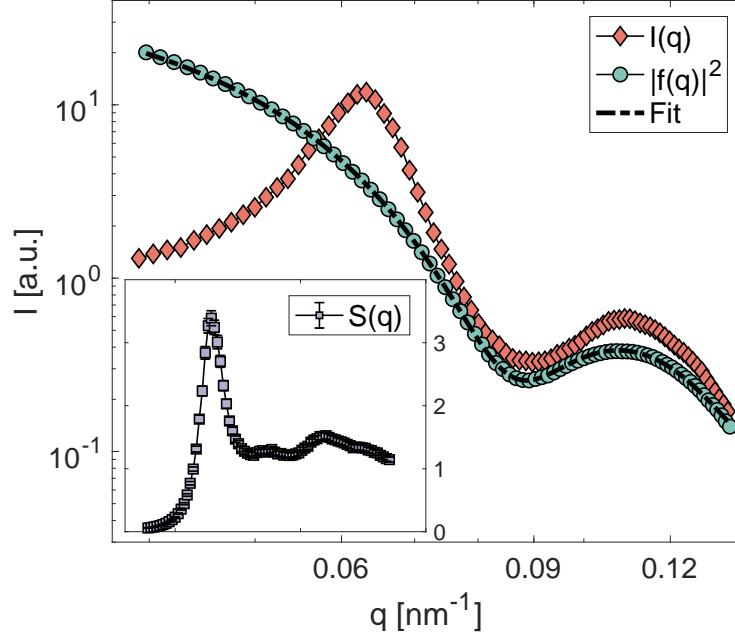
Fig. S2. Scattered intensity, form factor, and structure factor. Scattered intensity from the sample (red diamonds) and from the reference diluted suspension (green circles). Inset: static structure factor $S(q) = I(q)/|f(q)|^2$.

a set of normalised $g_2(q,t) - 1$ are reported, computed using the detector pixels in horizontal sectors at different values of q. These data can be well approximated by a KWW function (*11*)

$$g_2(q,t) - 1 = \alpha(q) \, \exp(-2(t/\tau)^\beta) \tag{7}$$

This function was fitted to the measured data, as shown in an example reported in Fig. S4A. As outlined in the main text, the shape of the autocorrelation functions is independent of q and can be described as a compressed exponential with $\beta \sim 2$. In Fig. S4B the $g_2(q,t) - 1$ for different ϕ and fixed q are reported. It is clear that approaching the vertical direction ($\phi = \pi/2$) both the relaxation time τ and the shape strongly change since $1/\tau = q \cdot \delta v \cdot \cos(\phi)$, as discussed in the main text. It is possible to notice that at some q values small oscillations can be found in the tail of the $g_2(q,t) - 1$ function. These features provide information on the distribution of the relative velocity field lying in the horizontal plane, similarly to what reported in XPCS experiments on
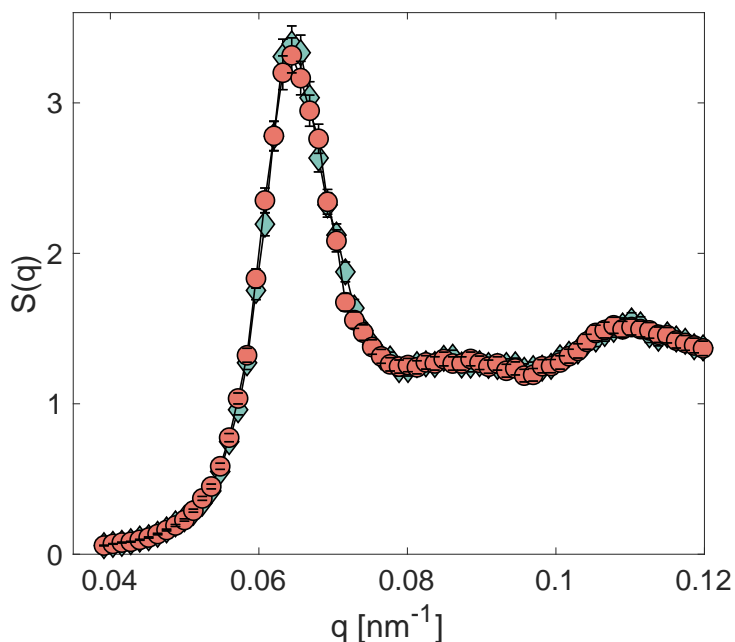
Fig. S3. Structure factor at different ages. Structure factor corresponding to the first and last frame of the measurements reported in the main text, showing that no significant structural changes have occurred in this period of time.

flowing colloidal suspensions (*44, 45*). As already observed in (*46*), the dynamics that we probe here arises solely from velocity differences between the particles in the scattering volume.

# Section S4. Dynamics, residual stresses, and gravity in colloidal glasses

Glasses, and colloidal glasses in particular, are expected to display a frozen dynamics on the experimental timescale (*23*). Still, since the first report of a compressed dynamics in colloidal gels (*17*), evidences accumulate that this is not the case, e.g. (*3, 12–16, 21*). This dynamics is usually related to the release of stress accumulated in the glass. Models (*17, 18*) and, more recently, numerical simulations make this connection clear (*19, 20*). From an experimental point of view, to the best of our knowledge, it has not been possible yet to measure directly the amount of stress accumulated locally in bulk glasses, and in particular in the colloidal glasses under dis-
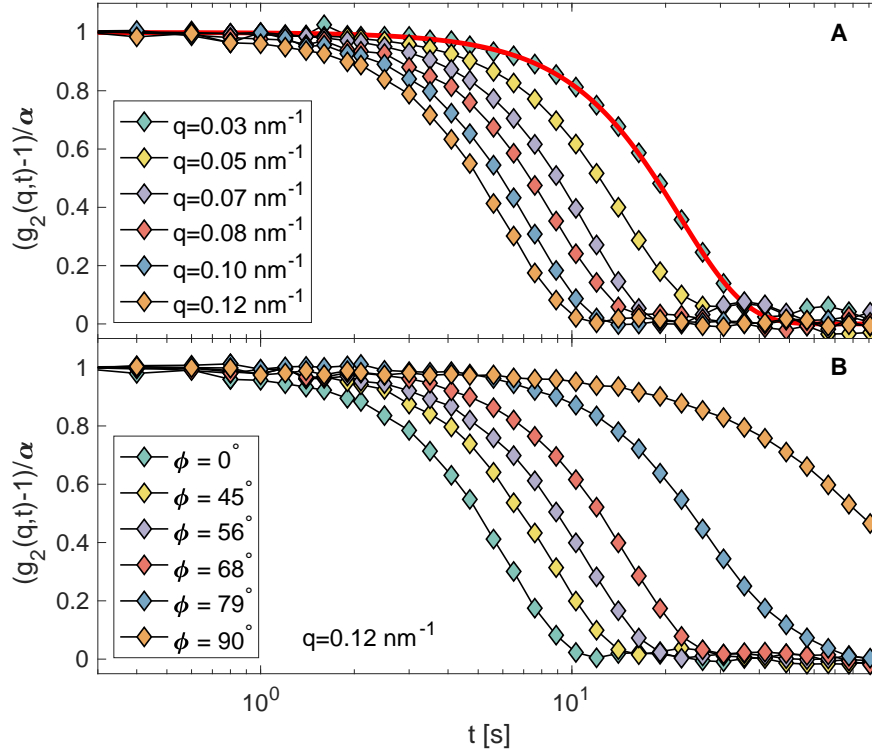
Fig. S4. Autocorrelation functions for different exchanged wave vectors and different azimuthal angles. A) Normalised intensity autocorrelation functions at different exchanged wavevectors computed selecting only horizontal sectors of the detector images (within the $\Delta\phi = \pi/16$ range). The red line is an example of fit to the data using a KWW ansatz. **B)** Normalised $(g_2(q,t) - 1)/\alpha$ functions at different azimuthal angles ϕ for a given q. These curves have been computed averaging over the $\Delta\phi = \pi/16$ range.

cussion here. However, indirect evidences of the connection residual stress-compressed exponential dynamics are abundant. The most important ones are the following: i) The compressed dynamics is present in the glassy state but disappears as soon as the non-equilibrium glassy state is turned into an equilibrium system either by changing the temperature (e.g. heating up a metallic glass across the glass transition temperature (*16*)) or the volume fraction (e.g. reducing the volume fraction in a colloidal glass below the arrested state limit (*24*)). ii) The characteristic time of this compressed dynamics increases when the glass ages, e.g. (*17*), suggesting that this
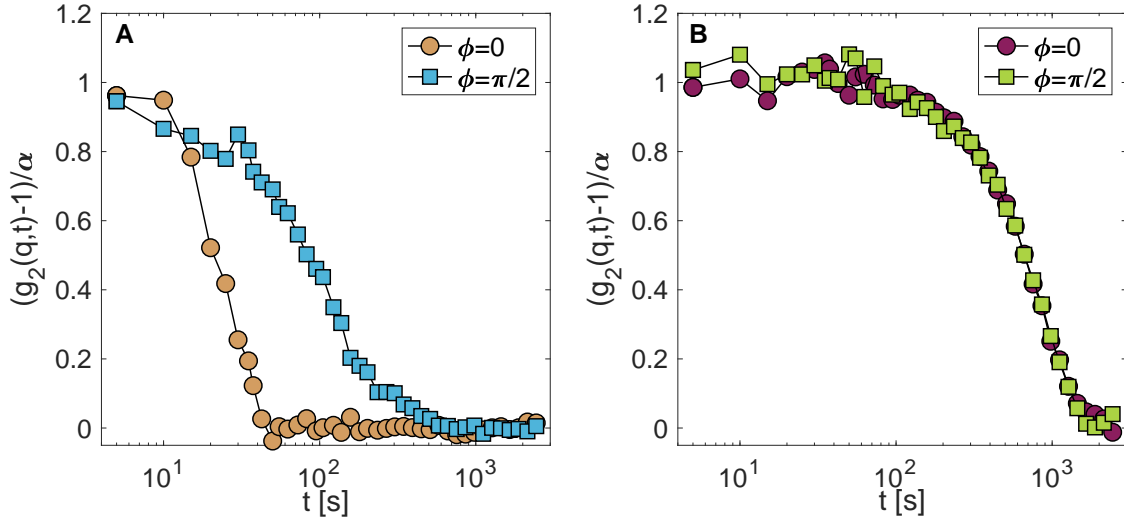
Fig. S5. **Effect of annealing on the dynamics probed in a colloidal glass.** Normalized intensity autocorrelation functions for different azimuthal angles for **A)** an as-prepared and **B)** an annealed sample. The as-prepared sample has been prepared as described in the Methods, and corresponds to a volume fraction $\varphi \sim 37$ %. The annealed sample is the same sample after heating it up to T=308 K for 20 min and then cooling it back to room temperature. These curves correspond to an exchanged wavevector q=(0.150 $\pm$ 0.015) nm^{-1} and have been computed selecting horizontal and vertical sectors of the detector images (see legend) within the $\Delta\phi = \pi/4$ range.

characteristic time scales inversely to the residual amount of stress. The samples discussed here make no exception to these observations, and their compressed dynamics clearly depends on the sample preparation protocol. It is for example possible to produce by annealing at higher than ambient temperature a colloidal glass which, while still displaying compressed exponential dynamics, shows a much longer characteristic time than at room temperature with no sign of anisotropy, see Fig. S5. This provides further support to the connection between local stress and compressed dynamics. Since the stress-induced dynamics observed here takes place in the horizontal plane, it is interesting to investigate the role possibly played by gravity. To this extent, a series of measurements were performed on the same sample in vertical and tilted alignment, see see Fig. S6. When tilting the capillary by $\phi_0 \approx 50°$ with respect to the vertical direction
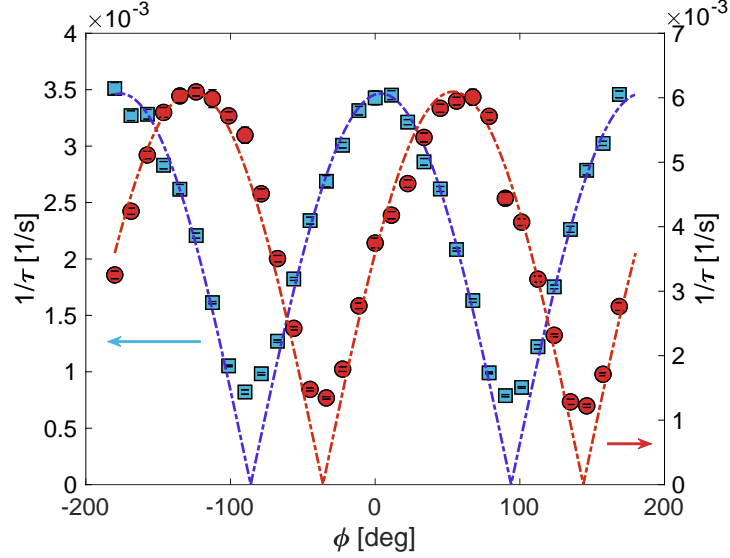
Fig. S6. Gravity does not affect the anisotropy of the dynamics. Azimuthal dependence of the relaxation rate for the as-prepared sample mounted vertically (blue squares, same conditions as in Fig. 2A of the main text) and for the same sample tilted by $\phi_0 \approx 50^o$ with respect to the vertical direction (red circles). The data for the tilted sample show a phase shift of ϕ_0 with respect to those for the vertical one. These data correspond to an exchanged wavevector $q=(0.124 \pm 0.012)$ nm^{-1} and have been computed selecting azimuthal sectors of the detector images within the $\Delta\phi = \pi/16$ range).

the argument of the cosine function that describes the relaxation rate, $\Gamma(\phi)$, is shifted by ϕ_0, implying that the velocity field (and therefore the stress field that gives rise to it) turns with the capillary and remains orthogonal to the capillary axis. This comparison shows that gravity plays a minor role in the development of the anisotropic dynamics discussed here.

Section S5. Dynamical heterogeneities

In order to study the length-scale of the dynamical processes discussed above, an observable sensitive to heterogeneities is required. One such observable is the four point correlation function defined as the variance of the intermediate scattering function $F(q,t)$ of Eq.4 (*23,28,47,48*)

$$\chi_4(q,t) = \langle (F(q,t) - \langle F(q,t) \rangle)^2 \rangle \tag{8}$$

This observable is in turn related to the variance of the two-times correlation matrix via Eqs. 2 and 3. It can be demonstrated (*23, 28, 47, 48*), that the $\chi_4(q,t)$ is a peaked function and that its maximum value is proportional to the number, N_r, of regions that move cooperatively within the scattering volume, though the presence of a q-dependent pre-factor does not allow providing a very precise estimate (*26*). However, by multiplying the $\chi_4(q,t)$ function for the total number of particles in the scattering volume, N, and observing that the number of particles that move cooperatively is $N_{corr} = N/N_r$, it is possible to estimate N_{corr} from the knowledge of N and $\chi_4(q,t)$ (*29,47,48*). Clearly, the $\chi_4(q,t)$ signal will be larger the smaller is the scattering volume and/or the larger are the regions displaying cooperative motion.

As illustrated in Ref. (*21*), the variance of the $g_2(q,t) - 1$ function, $\sigma_{g_2}^2$, computed from the two-times correlation matrix does not correspond exactly to the $\chi_4(q,t)$ defined in Eq. 8. In fact, the finite size of the statistical ensemble (which is directly proportional to the number of pixels, N_p) over which the intensity correlations are calculated introduces a statistical noise contribution (σ_n^2) that adds up to the intrinsic fluctuations due to the dynamical heterogeneities

$$\sigma_{g_2}^2(N_p, t) = \sigma_n^2(N_p, t) + \chi_4(q, t) \tag{9}$$

It can be demonstrated (*21*) that this noise term σ_n^2 decreases with the inverse of the number of pixels employed for the computation of the intensity correlations, eventually vanishing only in the limit $N_p \to \infty$. In the case of not too large speckle size to pixel size ratio $\sigma_n^2(N_p, t) \propto 1/N_p$. Thus an extrapolation scheme can be implemented to obtain $\chi_4(q,t)$ based on the computation $\sigma_{g_2}^2(N_p, t)$ for different N_p values, as shown in the example reported in Fig. S7. It has to be noticed that this extrapolation scheme requires a meaningful statistics and good signal to noise ratios for all the chosen N_p values, and so it cannot be applied for too low detected intensities (typical situation for ROIs corresponding to large q-values far from the structure factor's peak) or too low initial number of pixels (ROIs too small or too close to the direct beam).
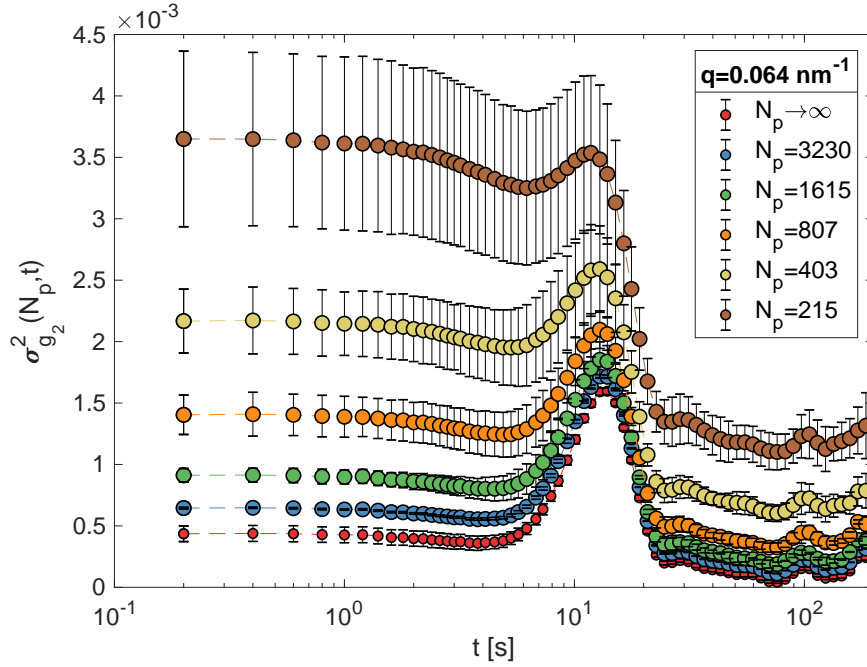
Fig. S7. Variance of the intermediate scattering function for different subensembles of detector pixels. Sequence of $\sigma^2_{g_2}(N_p, t)$ for $q = 0.064$ nm^{-1} and for the N_p values reported in the legend. The correct $\chi_4(q, t)$ (red circles) is obtained extrapolating the intensity in each time channel of these curves in the limit $N_p \to \infty$.

In the present case, the choice of the azimuthal range $\Delta\phi$ over which calculating the $\chi_4(q, t)$ function has to be the result of a compromise. In fact, on the one hand the $\Delta\phi$ range should be large enough to provide a good enough signal to noise ratio to correctly compute the $\chi_4(q, t)$ function; on the other hand, since the dynamics here studied is strongly anisotropic as it is confined in the horizontal plane, a too large $\Delta\phi$ range would clearly wash out the $\chi_4(q, t)$ signal. These effects are shown in Fig. S8, where a comparison of the $\chi_4(q, t)$ signal computed using different $\Delta\phi$ ranges is reported. Fig.S8 also shows that our choice of the $\Delta\phi = \pi/2$ range used to compute the $\chi_4(q, t)$ signal reported in the main text is a reasonable one, and highlights that neglecting possible anisotropies in the dynamics can effectively wash out the $\chi_4(q, t)$ signal.
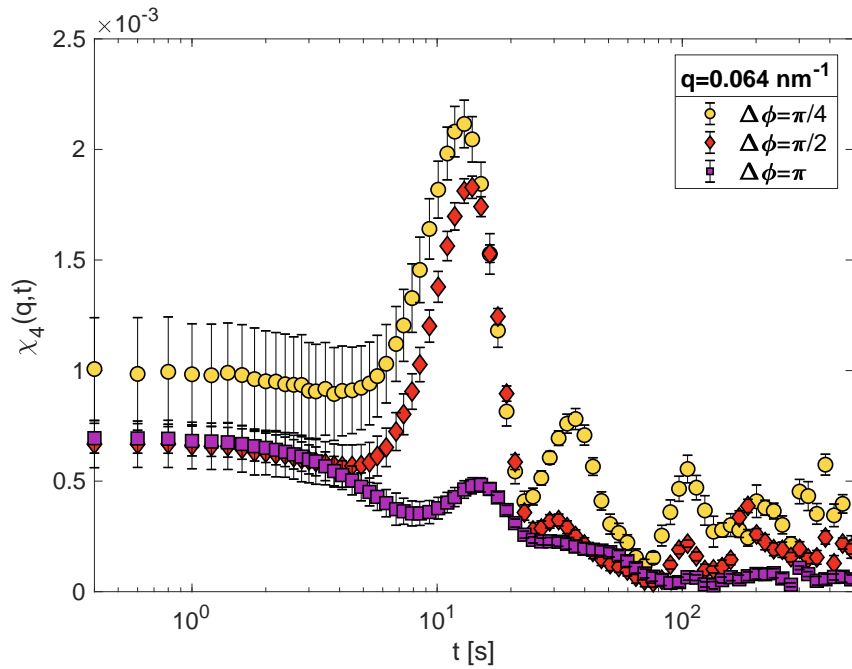
Fig. S8. Extrapolated variance of the intermediate scattering function for different ranges of azimuthal angles. Extrapolated dynamical susceptibility at $q = 0.064$ nm^{-1} computed using the horizontal sectors over different ranges: $\Delta\phi = \pi/4$, $\Delta\phi = \pi/2$, and $\Delta\phi = \pi$ (i.e. corresponding to the whole ring), see legend for correspondence to symbols. For $\Delta\phi = \pi$ the main peak of the $\chi_4(q,t)$ is clearly washed out, while for $\Delta\phi = \pi/4$ it has reached a basically stable value but the noise level starts to be relevant. $\Delta\phi = \pi/2$ is our best choice, and is the range used for the discussion in the main text.